# Crystalline and amorphous calcium carbonate as structural components of the *Calappa granulata* exoskeleton

M. Katsikini[a*], E. Proiou[a], N. Vouroutzis[a], F. Pinakidou[a], E. C. Paloura[a], D. Smirnov[b],

M. Brzhezinskaya[c] and S. Ves[a]

[a] Aristotle University of Thessaloniki, School of Physics, Section of Solid State

Physics, 54124 Thessaloniki, Greece

[b] Institut für Festkörperphysik, Technische Universität Dresden, Physikgebäude,

Zellescher Weg 16, 01069, Dresden, Germany

[c] Helmholtz-Zentrum Berlin für Materialien und Energie, Albert-Einstein-Str. 15,

12489 Berlin, Germany

*Corresponding Author: katsiki@auth.gr; tel: (+30) 2310 998500

## Abstract

The exoskeleton of crustaceans consists of chitin biopolymers where the embedded inorganic biominerals, mainly $CaCO_3$, affect strongly its mechanical properties. Raman and Near Edge X-ray Absorption Fine Structure (NEXAFS) spectroscopies and Transmission Electron Microscopy (TEM) are applied to investigate the $CaCO_3$ structure in various parts of the *Calappa granulata* crab exoskeleton. The shape of the main Raman peak of $CaCO_3$ reveals the presence of two phases which are identified as calcite and amorphous calcium carbonate (ACC). The relative concentration of the two phases in various parts of the exoskeleton is determined from the area ratio under the corresponding peaks. The results of the Ca $L_{3,2}$-edge NEXAFS analysis are in line with the Raman findings, since the energy separation of peaks that appear in the lower

frequency region of the main $L_2$ and $L_3$ peaks due to crystal field splitting, is directly related to the percentage of the ACC phase in the total $CaCO_3$ mineral content. The C $K$-edge spectra are used for the determination of the extent of calcification of the exoskeleton. Furthermore, dark and bright field TEM images reveal the presence of nanocrystallites with an average size of 20 nm. The structure of the nanocrystallites, as derived from the Selected Area Electron Diffraction patterns, is calcite. The results suggest that ACC plays a structural role in the exoskeleton of *Calappa granulata*.

**Keywords:** *Calappa granulata*, NEXAFS spectroscopy, Raman spectroscopy, biomineralization, amorphous calcium carbonate, Transmission Electron Microscopy.

**Abbreviations:**

ACC: Amorphous Calcium Carbonate

AXT: astaxanthin

BF: Bright Field

CF: Crystal Field

DF: Dark Field

FWHM: Full Width at Half Maximum

NEXAFS: Near Edge X-ray Absorption Fine Structure

SAED: Selected Area Electron Diffraction

TEM: Transmission Electron Microscopy

XRD: X-ray diffraction

## 1. Introduction

The excellent mechanical properties of hard tissues are attributed to biomineralization which is mainly driven by the necessity for a specific function, as for example support or protection. Contrary to vertebrates that possess a bone endoskeleton, crustaceans, like crabs, have exoskeletons that stabilize and protect the body (Hadley, 1986; Luquet, 2012). The exoskeleton is a nanocomposite material consisting of mainly $CaCO_3$ minerals embedded in the organic matrix network formed by $\alpha$-chitin-protein fibers arranged in a twisted plywood structure (Bouligand, 1972; Luquet, 2012; Nagasawa, 2012). Cuticle hardening is achieved by both sclerotization and calcification. The former refers to the formation of cross-linkages between the chitin fibers which are covered by protein and is the main hardening mechanism in all the arthropods. The latter occurs in most of the crustaceans where variation of the composition, symmetry, size and shape of the $CaCO_3$ crystallites permits control of the mechanical properties of parts of invertebrates' exoskeleton, like jaws, claws, and carapaces. For these reasons and due to the periodical synthesis and resorption of calcified structures in crustaceans, they are extensively studied and considered as models in biomineralization research (Luquet, 2012).

In aquatic organisms, $CaCO_3$ is commonly found in three crystalline polymorphs: calcite, aragonite and vaterite (Lowenstam, 1981). However, amorphous calcium carbonate (ACC) has been also detected in several different species (Aizenberg *et al.*, 1996; Beniash *et al.*, 1997; Hasse *et al.*, 2000; Levi-Kalisman *et al.*, 2002; Mergelsberg *et al.*, 2019; Weiss *et al.*, 2002). Biogenic ACC usually contains significant amounts of Mg and phosphate (Weiner *et al.*, 2003). Its amorphous character is deduced from the absence of well-defined peaks in the X-ray diffraction

(XRD) patterns and discrete CaCO$_3$ lattice modes in the low-frequency part of the Raman spectrum (Wehrmeister *et al.*, 2011. It has been proposed that ACC is a precursor of crystalline phases like aragonite or calcite (Addadi et al, 2006; Gong *et al.*, 2012; Raz *et al.*, 2000; Weiss *et al.*, 2002) and that it is a mean to facilitate resorption and recycling of cuticular calcium carbonate (Neues *et al.*, 2011). In many cases it coexists with CaCO$_3$ crystalline phases (Aizenberg *et al.*, 1996; Beniash *et al*., 1997; Mergelsberg *et al.*, 2019; Wehrmeister *et al.*, 2011; Weiss *et al.*, 2002). In addition, various ACC phases have been detected with distinct short-range order that is termed as polyamorphism in analogy to the polymorphism observed in crystalline CaCO$_3$ (Cartwright *et al.*, 2012). In sea urchin spicules, two amorphous mineral phases have been identified along with the crystalline phase of calcite (Gong *et al.*, 2012; Politi *et al.*, 2008): type 1 ACC, which is a hydrated form of ACC (ACC·H$_2$O) and type 2 which is the anhydrous. The ACC·H$_2$O $\rightarrow$ ACC $\rightarrow$ calcite transformation has been proposed in this type of biomaterial.

In this study, we apply Raman and Near Edge X-ray Absorption Fine Structure (NEXAFS) spectroscopies as well as Transmission Electron Microscopy (TEM) for the study of the calcium carbonate phases present in the exoskeleton of *Calappa granulata.* The cuticle of this crab exhibits characteristic red-orange color with dark red spots. Coloration in crustaceans is a visual cue that plays an important role in communication, interaction, sexual and agonistic behaviors (Baldwin and Johnsen, 2009). The orange color of crustaceans, e.g. crab and lobster, has been attributed to astaxanthin (AXT) which is a carotenoid chromophore (Buchwald *et al.*, 1968; Cianci *et al.*, 2002; Salares *et al.*, 1977a; Tilley, 2011). The presence of AXT in the crustacean's exoskeleton can be easily identified by Raman spectroscopy as it

provides intense bands at approximately 1500, 1150 and 1000 cm$^{-1}$ (Rivera *et al.*, 2012). Raman spectroscopy, as a non-destructive technique, has been also applied for the unambiguous discrimination of crystalline and non-crystalline phases of CaCO$_3$ and for the detection of phosphates (Jacob *et al.*, 2011; Hasse *et al.*, 2000; Hild *et al.*, 2008; Raz *et al.*, 2000; Wehrmeister *et al.*, 2011). The position, splitting and Full Width at Half Maximum (FWHM) of the $\nu_1$ stretching mode of $CO_3^{2-}$, at *ca.* 1080 cm$^{-1}$, is a safe fingerprint of the amorphous or crystalline state of CaCO$_3$. On the other hand, the lattice modes that appear in the low-frequency part of the Raman spectrum can be safely used for the identification of the crystalline CaCO$_3$ polytypes, as they are mostly affected by the symmetry of the crystal (Nehrke *et al.*, 2012). NEXAFS spectroscopy is also applied for the study of calcified tissues (Konashuk *et al.*, 2018; Pavlychev et al., 2016; Petrova *et al.*, 2017). It is element specific and probes the partial density of empty electronic states providing information on the local bonding configuration and symmetry (Stöhr, 2003). More specifically, the NEXAFS spectra recorded at the C *K* absorption edge probe the electronic transitions from the C 1s initial state to final states with p component which are sensitive to the bonding configuration of carbon (Benzerara *et al.*, 2014). In the Ca $L_{3,2}$-edge NEXAFS spectra, the dominant transitions are 2p$_{3/2,1/2}\rightarrow$ 3d (Cosmidis *et al.*, 2015). The NEXAFS spectrum is very sensitive to the local bonding of Ca because of the modification of the d-electronic states by the crystal field (de Groot and Kotani, 2008). Direct observation (shape, size, orientation) of the biomineral crystallites can be achieved by TEM whereas Selected Area Electron Diffraction (SAED) is used for the identification of the crystal structure of the nanocrystals (Klepal *et al.*, 2010; Seidl *et al.*, 2012; Štrus *et al.*, 2019; Vittori *et al.*, 2012).

## 2. Materials and methods

The male *Calappa granulata* crab was obtained from a local seafood supplier. It was collected in the North Aegean Sea and it was in the intermolt stage (the basal membrane on the inner surface of the cuticle was present) (Waddy *et al.*, 1995). After removing the soft tissue from the inner part, the exoskeleton was washed with water, left to dry and stored in air. A photograph of the studied crab is shown in Fig. 1. Raman spectra were recorded from selected spots of the crab exoskeleton (carapace: C1–C3, M1, R1; palm: RP1–RP4; carpus: RC1; finger: RF1, RF2; leg: RL1, RL2) which are indicated in Fig. 1. Raman spectra were also recorded from spots belonging to exoskeleton parts from where the NEXAFS spectra were acquired (spots 1-15 in Fig. 1). For the NEXAFS measurements, various portions of the exoskeleton were cut and crushed to prepare a fine powder that was pressed on a scratched In foil to eliminate charging effects. A crystalline calcite sample was used as reference (Zougrou *et al.*, 2016). The NEXAFS spectra were recorded under ultra-high vacuum conditions ($\sim5\times10^{-10}$ Torr) using the photocurrent signal at the C *K*- and Ca *L*$_{3,2}$-absorption edges at the Russian-German beamline of the BESSY-II Storage Ring facility of the Helmholtz Zentrum Berlin (Molodtsov *et al.*, 2009). They were normalized by the signal of a gold grid with high transmissivity positioned in front of the sample in order to take into account the transmission function of the monochromator.
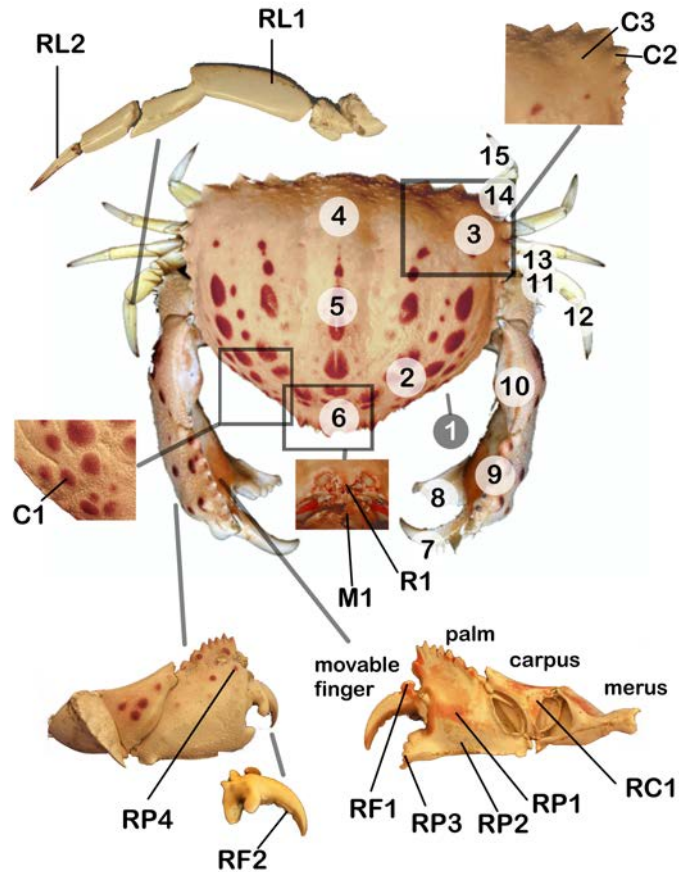
***Figure 1: Photograph of the studied Calappa granulata crab and parts of the exoskeleton.*** *Spectra were recorded from points 1-15 (NEXAFS) and 1-15, RPi, RFi, RC1, M1, R1, Ci, RLi (Raman).*

The Raman spectra were recorded in the backscattering geometry using a RAMALOG-5 system equipped with a triple monochromator and a Peltier-cooled photomultiplier. For the excitation, the blue line of an Ar+ ion laser ($\lambda$=488 nm) was used and the spectral resolution was *ca.* 2 cm$^{-1}$. The beam was focused using a spherical lens with f=10 cm and the spot diameter on the sample was approximately 1 mm. Monochromator shifts were corrected using the Ar$^{+}$ laser plasma lines. TEM images were recorded from pos. 5 (carapace) shown in Fig. 1, using a 100 kV JEOL 100CX microscope. The samples were prepared by scratching.

## 3. Results

### 3.1. Transmission Electron Microscopy

Optical microscopy images recorded from cross sections of the top of the carapace (pos. 5) are shown in Fig. 2(a). Bright (BF) and Dark Field (DF) TEM images as well as SAED patterns are shown in Fig. 2(b,c). The optical microscopy image [Fig. 2(a)] reveals a lamellar structure which is characteristic of the endocuticle and cannot be resolved in the exocuticle, most probably due to denser stacking (Chen *et al.*, 2008). The exocuticle is interrupted by parts of the endocuticle that bulge out [marked with "B" in Fig. 2(a)] in distal direction. The undisturbed exocuticle region is marked with "A". The BF, DF images and SAED patterns recorded from the A and B regions are shown in Fig. 2(b) and (c) in the left, right and middle panel, respectively. The BF and DF images of region A reveal the presence of crystallites with an average size of 20 nm, verifying the nanocrystalline character of the inorganic constituent. In region B, the lamellar structure is prominent also at the nano-level. The SAED patterns from both the A and B regions are characteristic of calcite. However, in region A, the nanocrystallites appear randomly oriented, as it is deduced from the rings observed in the SAED pattern, whereas in region B they exhibit preferential orientation.
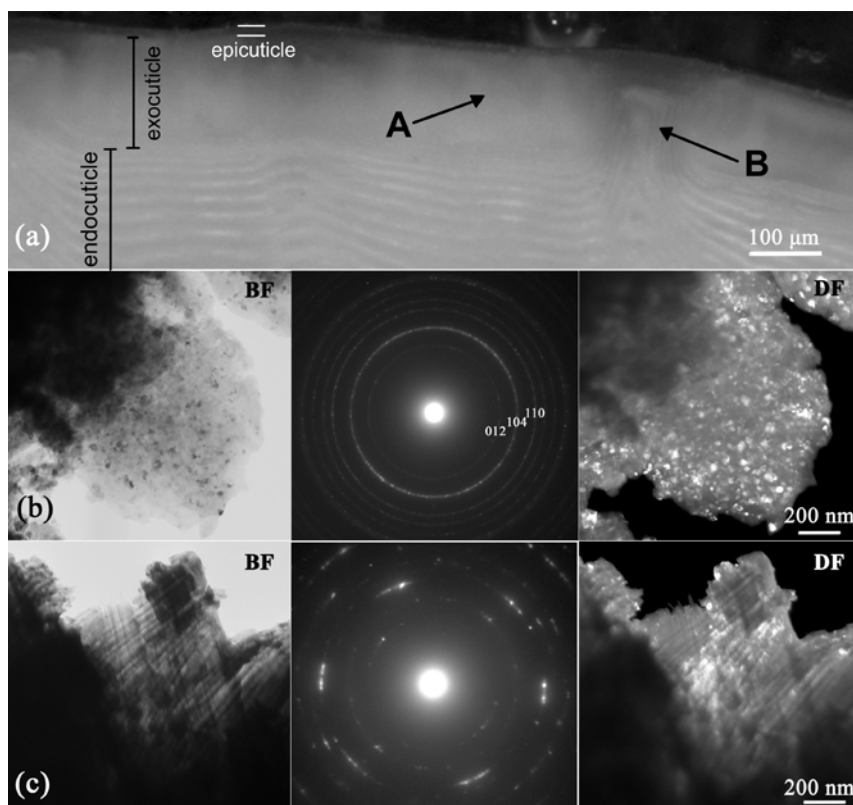
8

*Figure 2: Optical and electron microscopy images of part of the carapace. (a) Cross section optical microscopy image which shows the regions of endo-, exo- and epicuticle. Bright (BF), dark (DF) field TEM images and corresponding Selected Area Electron Diffraction (SAED) patterns recorded from regions A and B, are shown in (b) and (c) on the left, right and middle panel, respectively.*

## 3.2. NEXAFS spectroscopy

### 3.2.1. C *K*-edge

Representative C *K*-edge NEXAFS spectra that were recorded from different parts of the exoskeleton are shown in Fig. 3(a). Peaks due to C 1s $\rightarrow$ 2$\pi$* transitions are prominent in the energy range 285-292 eV and their positions are indicated by vertical lines. The peaks were named according to the notation adopted by Benzerara *et al.* (2004). More specifically, the features a*, k*, p*, cx*, cn* appear at 285.2, 286.8, 288.2, 288.5 and 290.3 eV, respectively, and correspond to aromatic, ketonic/phenolic, amide carbonyl (peptide), carboxylic and carbonate species, respectively. The area under the p* and cx*peaks, $A_{p*,cx*}$, due to transitions of the

C=O bonds in proteins and/or the chitin polymer, can be considered proportional to the organic component of the exoskeleton while the area under the cn* peak, $A_{cn}$, is proportional to the (calcium carbonate) inorganic constituent. Therefore, a calcification ratio can be defined as:

$$R_{carbonate} = \frac{A_{cn*}}{A_{cn*} + A_{p*,cx*}} \qquad (1)$$

and can be taken as a relative measure of the calcium carbonate content in various parts of the exoskeleton.

To determine the areas under the peaks, the spectra were fitted using a sigmoidal and Gaussian functions to take into account the transitions from the 1s initial state to final states with p component in the continuum and to final bound states, respectively (Lam *et al.*, 2012). A representative fitting is shown in Fig. 3(a). The $R_{carbonate}$ values for the examined exoskeleton regions are listed in Table 1. A rough $R_{carbonate}$ color map of the exoskeleton is shown Fig. 3(b). Red regions correspond to more extended calcification whereas blue ones to regions with a lower $CaCO_3$ content. It should be pointed out, that $R_{carbonate}$ does not provide the exact percentage of C that participates in the formation of calcium carbonate, but it is rather proportional to that percentage, because the transition probabilities are not necessarily the same for all considered 1s $\rightarrow \pi*$ transitions. The map reveals that higher calcification ratios occur at the end of the claw whereas the leg tips are less calcified. Variations are also observed on the carapace.
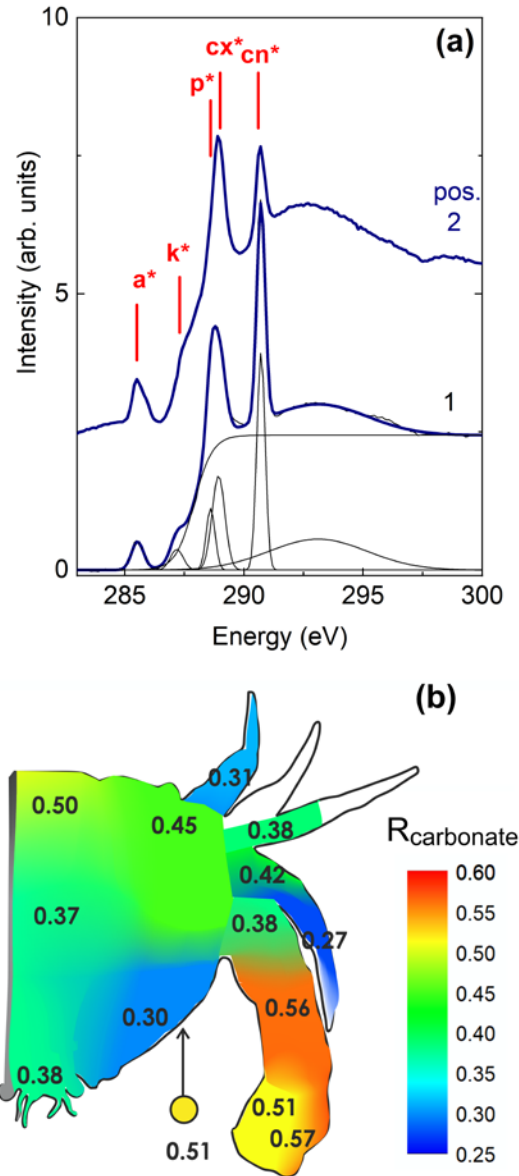
*Figure 3: C K-edge NEXAFS spectra and calcification map. (a) Representative C K-edge NEXAFS spectra recorded from ventral (pos.1) and dorsal (pos.2) part of the exoskeleton. Vertical lines indicate the position of the 1s → π\* transitions denoted according to Benzerara et al. (2004). A representative fitting is shown for the spectrum recorded from pos. 1 using a step function and a number of Gaussians that simulate the transitions to the continuum and to bound states, respectively. (b) Color map of the calcification ratio, R$_{carbonate}$. The R$_{carbonate}$ values are also shown on the map.*

### 3.2.2. Ca $L_{3,2}$-edge

The Ca $L_{3,2}$-edge NEXAFS spectra are dominated by 2p → 3d transitions of the Ca atom. The spin-orbit interaction results in two main absorption features separated by

*ca.* 3.3 eV (Spin-Orbit Splitting) corresponding to the $2p_{3/2}$ ($L_3$) or $2p_{1/2}$ ($L_2$) initial state. Crystal field (CF) interactions induce further splitting of each $L$-edge main peaks causing the appearance of an intense peak or shoulder in the low energy region of each main peak. The Ca $L_{3,2}$-edge spectrum of a reference crystalline calcite sample is shown in Fig. 4. The peak notation is according to Fleet and Liu (2009). The Ca $L_{3,2}$-edge spectrum can be simulated utilizing atomic multiplet calculations to take into account the $2p$-$3d$ and $3d$-$3d$ Coulomb and exchange interactions, the $2p$ and $3d$ spin-orbit interactions and the crystal field acting on the $3d$ states (de Groot *et al.*, 1990). In calcite (space group R-*3m*), $Ca^{2+}$ has a site symmetry of $\overline{3}$ and is 6-fold (octahedrally) coordinated with O atoms belonging to the planar $CO_3^{2-}$ ions. In aragonite (space group P*mcn*), $Ca^{2+}$, with site symmetry *m*, is 9-fold coordinated with O atoms. The larger polyhedron of Ca in aragonite, compared to calcite, results in weaker crystal field, which is further reflected in the intensities as well as in the separation of the $a_1$ and $b_1$ peaks from the main $a_2$ and $b_2$ peaks, respectively (Fleet and Liu, 2009). More specifically, the energy differences $a_2$-$a_1$ ($L_3$ splitting) and $b_2$-$b_1$ ($L_2$ splitting) are 1.3 and 0.8, for calcite and aragonite, respectively. The $b_2$-$a_2$ (Spin-Orbit Splitting) is not significantly affected, with values of 3.4 and 3.3 for calcite and aragonite, respectively. Finally, the 1 and 2 peaks also shift towards the main peaks in aragonite (Fleet and Liu, 2009).

The Ca $L_{3,2}$-edge spectra of the ACC·$H_2O$ and ACC phases are characterized by lower intensity of the $a_1$ and $b_1$ peaks compared to the crystalline calcite counterpart, with the $a_2$ being more intense in the dehydrated ACC phase (Gong *et al.*, 2012; Politi *et al.*, 2008). However, a recent study on the phase transformation process of hydrated ACC, suggests that the type-2 ACC phase is not the anhydrous phase of type-1 ACC

but rather a disordered calcium carbonate phase identified in nanoparticles, with calcitic structure at the nanometer scale. The reported values of the $L_3$ and $L_2$ splitting for commercial nanocalcite are 1.07 and 1.11, respectively (Tsao *et al.*, 2019).

***Table 1:*** *Calcification ratios, $R_{carbonate}$, and $L_2$, $L_3$ crystal field and Spin-Orbit splitting of different exoskeleton regions. The calcification ratios, $R_{carbonate}$, were determined from the C K-edge NEXAFS spectra as discussed in Section 3.2.1 and the rest of the parameters from the Ca $L_{3,2}$–edge spectra, discussed in Section 3.2.2.*

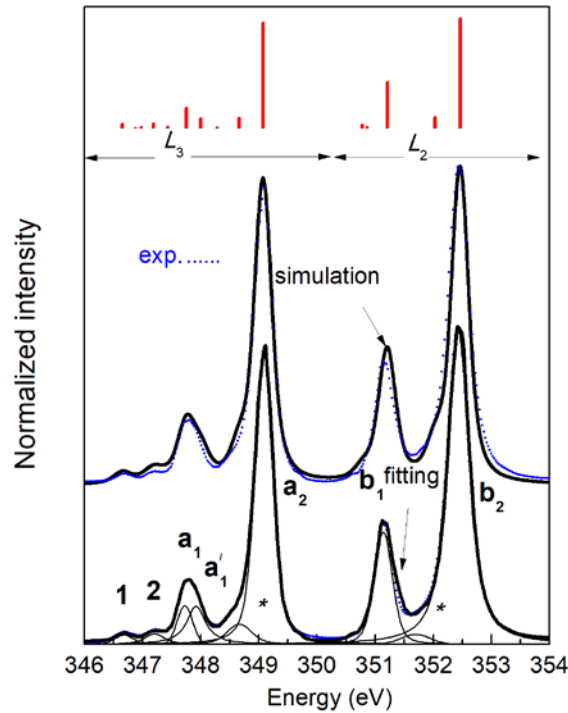| Sample region | $R_{carbonate}$ ±0.02 | $L_3$ Splitting ±0.02 (eV) | $L_2$ Splitting ±0.01 (eV) | Spin-Orbit Splitting ±0.01 (eV) |
|---|---|---|---|---|
| calcite | - | 1.27 | 1.28 | 3.35 |
| 1 | 0.51 | 1.16 | 1.15 | 3.32 |
| 2 | 0.30 | 1.13 | 1.14 | 3.34 |
| 3 | 0.45 | 1.14 | 1.12 | 3.31 |
| 4 | 0.50 | 1.18 | 1.17 | 3.34 |
| 5 | 0.37 | 1.14 | 1.09 | 3.31 |
| 6 | 0.38 | 1.16 | 1.14 | 3.32 |
| 7 | 0.57 | 1.21 | 1.18 | 3.32 |
| 8 | 0.51 | 1.17 | 1.15 | 3.33 |
| 9 | 0.56 | 1.19 | 1.14 | 3.31 |
| 10 | 0.38 | 1.20 | 1.15 | 3.31 |
| 11 | 0.42 | 1.17 | 1.15 | 3.32 |
| 12 | 0.27 | 1.15 | 1.14 | 3.31 |
| 13 | 0.38 | 1.16 | 1.14 | 3.33 |
| 14,15 | 0.31 | 1.14 | 1.12 | 3.34 |

***Figure 4: Fitting and simulation of the Ca*** $L_{3,2}$***–edge NEXAFS spectrum of a crystalline calcite sample****. The experimental spectrum is shown in blue dotted line whereas the simulation and the fitting curves in thick solid lines. Voigt functions were used for the fitting while for the simulation, the CTM4XAS software was employed. The peaks marked with asterisks were necessary to improve the fitting quality and can be substantiated by the simulation. Vertical red lines indicate the positions and the relative intensities of the lines predicted by the CTM4XAS multiplet calculations.*

The spectrum of crystalline calcite was fitted using Voigt functions, as indicated in Fig. 4. Except from the expected peaks 1,2,$a_1$, $a_2$, $b_1$, $b_2$ (Fleet and Liu, 2009), three additional peaks, marked with $a'_1$ and asterisks, were necessary to take into account the asymmetry of the main peaks, which became evident due to the good spectral resolution of the beamline. Such asymmetries were also revealed in the simulations performed using the CTM4XAS code for multiplet calculations (Stavitski *et al.*, 2011), if a $D_{4h}$ symmetry is used (with 10Dq = 1.10 eV, Ds = -0.07 eV, Dt = 0)

instead of the $O_h$ symmetry that accounts for an undistorted octahedron around Ca. Although the Ca-O distances in the calcite octahedron are equal, the O-Ca-O angles slightly deviate from $90^o$ (Rez *et al.*, 2011). The simulation shown in Fig. 4 corresponds to Lorentzian and Gaussian broadening of 0.1.

Representative NEXAFS spectra that were recorded from different positions of the exoskeleton are shown in Fig. 5. The spectra were energy shifted to allow for the $b_2$ peak to coincide with the corresponding peak of calcite. They were also subjected to a double step (sigmoidal function) subtraction (one for each of the $L_2$, $L_3$ edges). To facilitate comparison, the spectrum of the calcite reference sample, shown in red line, is also included in Fig. 5. The spectrum recorded from the claw finger (pos. 7) matches closely the spectrum of the crystalline calcite whereas the spectra recorded from other positions (5, 10, 12) exhibit strong deviations in the $L_2$, $L_3$ CF splitting ($a_2$-$a_1$ and $b_2$-$b_1$ separations). To determine the peak positions, the spectra were fitted using Voigt functions (30% Lorentzian – 70% Gaussian contribution). The $a_2$-$a_1$ and $b_2$-$b_1$ peak separations are listed in Table 1 along with the Spin-Orbit Splitting. The $L_3$ *vs.* $L_2$ splitting is plotted in Fig. 6 (lower panel) along with the corresponding splitting for the crystalline calcite, aragonite (Fleet and Liu, 2009), nanocrystalline calcite (Tsao *et al.*, 2019) and ACC (Gong *et al.*, 2012; Albéric *et al.*, 2019). An expanded view of the data for values of the $L_2$ splitting ranging from 0.7 to 1.4 eV is shown in the upper panel of the Figure. Variations are detected between the different parts of the exoskeleton. The observed values lie in-between the corresponding values for crystalline and nanocrystalline or amorphous calcite. Larger values of the $L_2$ and $L_3$ splitting are observed in the finger of the claw (pos. 7) while lower values were measured on the top of the carapace (pos. 5). The variation in the $L_2$ and $L_3$ splitting

15

values throughout the exoskeleton can be attributed to variations in the crystallite size

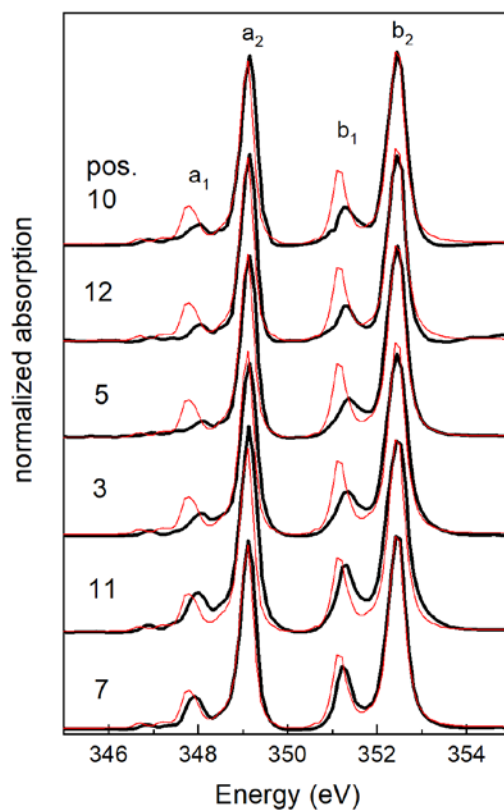and/or changes in the amorphous over crystalline calcium carbonate content.



***Figure 5: Ca L_{3,2}-edge NEXAFS spectra recorded from various parts of the exoskeleton.*** *The spectra recorded from the exoskeleton are plotted with thick black lines and are compared with the spectrum of a calcite reference sample which is plotted with thin red lines. Smaller peak separations ($a_2$-$a_1$ and $b_2$-$b_1$) due to CF splitting are observed in the spectra from regions with high amorphous content (pos. 5) compared to well crystallized regions (pos. 7) that exhibit higher splitting that is closer to the splitting in reference calcite sample.*
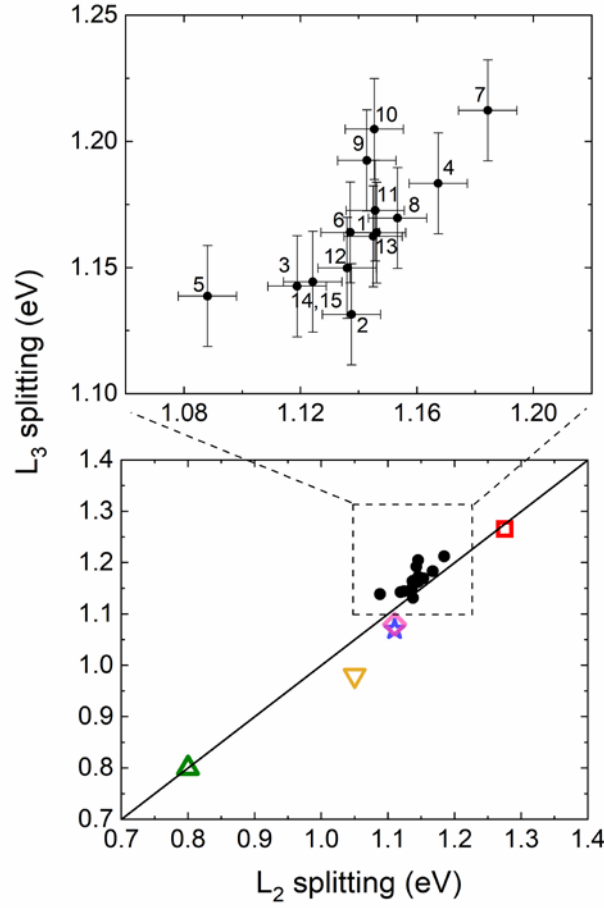
***Figure 6: L₃ vs. L₂ crystal field splitting of the Ca L₃,₂-edge spectra.*** *(bottom panel) L₃ vs. L₂ crystal field splitting of the spectra recorded from various parts of the exoskeleton (filled circles). Open red square, blue star, green up triangle, yellow down triangle and magenta rhomb correspond to the calcite reference sample, nanocalcite (Tsao et al., 2019), aragonite (Fleet and Liu, 2009), and ACC (Albéric et al., 2019; Gong et al., 2012), respectively. The y=x line is plotted in solid line. The part of the graph that corresponds to the crab data is magnified in the top panel where the numbers corresponding to various positions of the crab exoskeleton are shown in Fig.1.*

## 3.3. Raman spectroscopy

A representative Raman spectrum recorded from a colored part of the exoskeleton is shown in Fig. 7. Peaks owing to $CaCO_3$ as well as to astaxanthin (AXT) chromophore are detected. The peaks originating from the AXT chromophore appear at 960(*w*), 1007(*m*), 1156(*s*), 1193(*m*), 1273(*w*), 1320(*w*) and 1518(*s*) $cm^{-1}$ (Kaczor *et al.*, 2011; Katsikini, 2016; Penel *et al.*, 1998; Salares *et al.*, 1977a; Weesie *et al.*, 1999). The

most intense peak located at 1518 cm$^{-1}$ is assigned to the C=C bond stretching mode. Its frequency value depends on several parameters, such as the degree of conjugation and length of the polyene chain of the carotenoid molecule, the polarization induced by polar solvents and the planarity of the chain (Salares *et al.*, 1977a, 1977b; Weesie *et al.*, 1999). The second most intense peak at 1156 cm$^{-1}$ has contributions from both the C-C stretching mode of the polyene chain and from the in-plane C-H bending mode. The peak at approximately 1005 cm$^{-1}$ corresponds to CH$_3$ rocking vibrations. The strongest peak from CaCO$_3$, $v_1$, which is characteristic of vibrations of the CO$_3^{2-}$ ion, appears at 1087 cm$^{-1}$. The positions of this peak cannot be safely used for the identification of the calcite or aragonite polytypes because this mode enables vibrations of the CO$_3^{2-}$ ion (Nehrke *et al.*, 2012) present in both polytypes. However, due to the different crystal structure of the two polytypes (see discussion in Sect. 3.2.2), the lattice modes that appear in the low frequency part of the spectrum, can be considered as a fingerprint of the polytype structure. In the studied sample spots, where luminescence did not mask the Raman signal, a broad (with a FWHM of *ca.* 30 cm$^{-1}$) low-intensity peak centered at 280 cm$^{-1}$ was detected, verifying that CaCO$_3$ adopts the calcite structure (Behrens *et al.* 1995) in accordance with the NEXAFS and TEM results.

The inset of Fig. 7 shows the spectra recorded from different parts of the exoskeleton in the frequency range around the $v_1(\text{CO}_3^{2-})$ peak. The corresponding peak for crystalline calcite is also included. The large width of the $v_1(\text{CO}_3^{2-})$ peak in the spectra recorded from the crab, reveal that CaCO$_3$ forms nanocrystals or even an amorphous phase. In certain sample spots, the $v_1(\text{CO}_3^{2-})$ peak exhibits a prominent

asymmetry towards lower wavenumbers. To account for this asymmetry, the peak was fitted following the procedure proposed by Wehrmeister *et al.* (2011), i.e. two contributions were used, one Lorentzian lineshape (L), at approximately 1088 cm$^{-1}$, that corresponds to (nano)crystalline $CaCO_3$ and one Gaussian (G), located at approximately 1078 cm$^{-1}$, that corresponds to an ACC phase. Wehrmeister *et al.* (2011) applied this model to fit the $\nu_1(CO_3^{2-})$ peak in spectra recorded from bivalves, freshwater cultured pearls and woodlouse samples. Two contributions in the $\nu_1$ peak of the $CO_3$ ion were also detected in palm of the *Callinectes Sapidus* crab claw (Katsikini, 2016). The fitting results are listed in Table 2. In most of the spots of the *C. granulata* carapace two $CaCO_3$ phases are detected. The phase that is termed as crystalline is rather nanocrystalline as it can be deduced from the FWHM of the corresponding Raman peak that is 2.4-4.2 times larger than the FWHM of a crystalline calcite reference sample (3.6 cm$^{-1}$). The second phase is termed as amorphous due to the broader profile of the assigned peak (the FWHM ranges from 9 to 23 cm$^{-1}$) and/or its shift towards lower frequencies. The mode softening and the larger FWHM are induced by the structural disorder that causes relaxation or breakdown of the selection rules, enabling contributions from larger wavevector values, which in turn correspond to lower vibration frequency values.

Wehrmeister *et al.* (2011) defined the ratio of the areas under the peaks that correspond to the nanocrystalline and amorphous phases as the crystallinity index which can be used for the quantification of the two phases. However, this index cannot be defined in cases with null amorphous contribution. To alleviate this indeterminacy, here we define the crystallization ratio as the ratio of the nanocrystalline component relative to the total calcium carbonate content:

$$R_{cry} = \frac{A_{nc}}{A_{nc} + A_{am}}$$

<div align="right">(2)</div>

where, $A_{nc}$ and $A_{am}$ is the area under the peaks that correspond to the nanocrystalline and amorphous phases, respectively. The $R_{cry}$ values obtained for different exoskeleton parts are listed in Table 2. It can be deduced that in the spots from the claw finger and palm 100% crystallization occurs. In parts of the exoskeleton which are softer (e.g. top of the carapace), a considerable amount of amorphous phase is present. Furthermore, variations in the width of the Lorentzian peak are observed, implying that the calcite crystallite size also varies in different parts of the exoskeleton (Campbell and Fauchet, 1986). Smaller widths, associated with larger crystallite sizes, are observed in spots located in the finger and the palm (RF2, RP1).
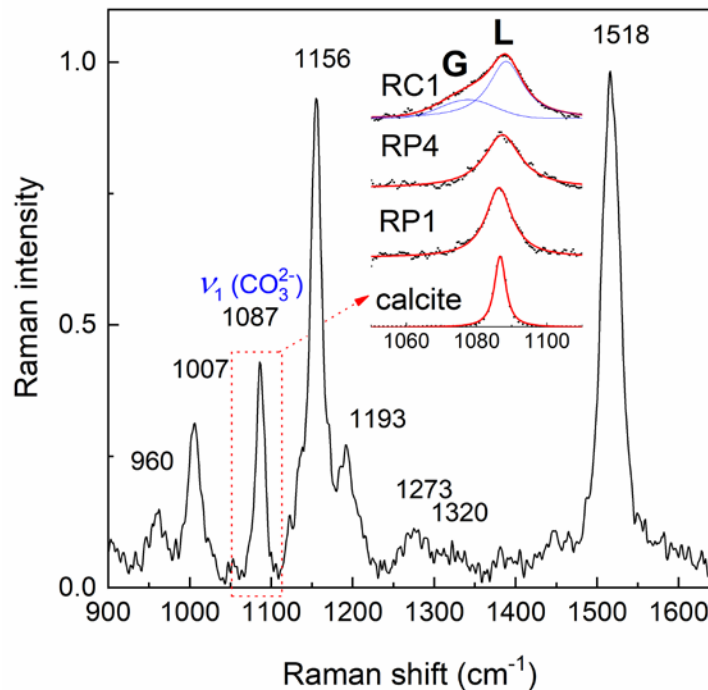


*Figure 7: Raman spectrum recorded from a pigmented part of the exoskeleton. The inset shows spectra around the most intense peak of CaCO₃, $v_1$ ($CO_3^{2-}$), acquired from three different parts of the claw, along with that of calcite.*

***Table 2:*** *Fitting results of the Raman spectra recorded from spots belonging to the same regions were the NEXAFS spectra were recorded (pos. 2-14,15) and from selected spots on the exoskeleton (see Fig. 1). The FWHM of the Lorentzian peak in* $cm^{-1}$ *is also provided in parentheses for the spots where only the Lorentzian contribution is observed.*

| Region/spot | Crystallization ratio | Region/spot | Crystallization ratio |
|---|---|---|---|
| RP1 | 1.00±0.00 (9.1±0.3) | 2 | 0.69±0.05 |
| RP2 | 1.00±0.00 (12.6±0.3) | 3 | 0.62±0.05 |
| RP3 | 0.91±0.02 | 4 | 0.81±0.03 |
| RP4 | 1.00±0.00 (14.9±0.4) | 5 | 0.59±0.05 |
| RC1 | 0.73±0.04 | 6 | 0.76±0.04 |
| RF1 | 0.83±0.03 | 7 | 0.87±0.03 |
| RF2 | 1.00±0.00 (9.1±0.3) | 8 | 0.77±0.04 |
| R1 | 0.76±0.04 | 9 | 0.76±0.04 |
| M1 | 0.68±0.05 | 10 | 0.80±0.04 |
| C1 | 0.56±0.06 | 11 | 0.74±0.04 |
| C2 | 0.62±0.05 | 12 | 0.66±0.04 |
| C3 | 0.61±0.05 | 13 | 0.82±0.03 |
| RL1 | 0.74±0.04 | 14,15 | 0.67±0.05 |
| RL2 | 0.66±0.05 | | |

In order to provide a means for the quantification of the ACC content using the Ca $L_{3,2}$-edge NEXAFS spectra, we plotted the crystallization ratio obtained with Raman spectroscopy against the $L_2$ crystal field splitting from Ca $L_{3,2}$-edge NEXAFS spectra (Fig. 8a). For that reason, Raman spectra were also recorded from central spots of the exoskeleton pieces from where NEXAFS spectra were also recorded. For completeness, we mention that an attempt to measure Raman spectra directly from the powdered samples used to measure the NEXAFS spectra was unsuccessful due to the intense luminescence-induced background. In general, white regions yielded much higher background compared to stained parts of the cuticle. The obtained equation, Y=-3.01+3.28·X (with R=0.902) can be used in order to determine the crystallization ratio (Y) from the characteristics of the NEXAFS spectra (X: $L_2$ splitting). A color map that roughly shows the crystallization ratio in various parts of the exoskeleton is included in Fig. 8(b). Higher crystallization ratios were identified at the claw finger while lower values correspond to the legs and the top of the carapace. It should be pointed out, that the Ca $L_{3,2}$-edge NEXAFS spectra provide average information from a specific exoskeleton segment because the experiment could only be conducted on powdered samples.
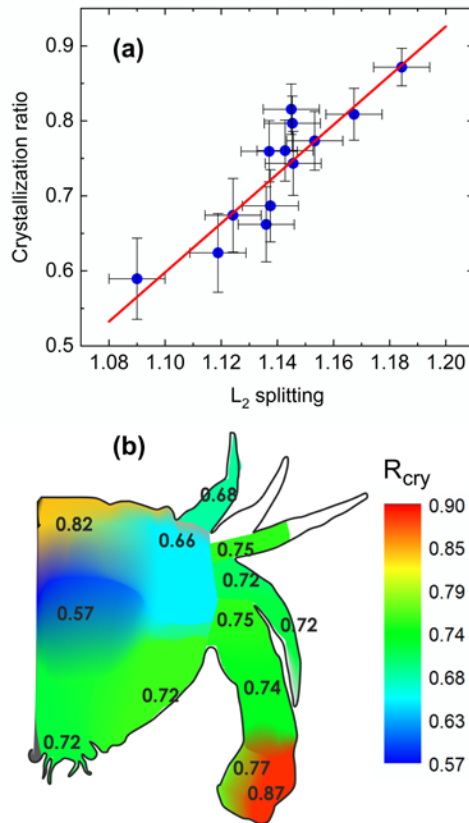
**Figure 8: Crystallizaton ratio dependence on the L₂ splitting.** *(a) Dependence of the crystallization ratio, $R_{cry}$, on the $L_2$ splitting as determined by Raman and Ca $L_{3,2}$-edge NEXAFS spectra, respectively. Blue circles correspond to spectra recorded from various positions of the exoskeleton (see Fig. 1). The red curve corresponds to linear fitting $(Y=-3.01+3.28 \cdot X)$, exhibiting a high degree of correlation. (**b**) Color map of the crystallization ratio as determined by the $L_2$ splitting and the polynomial fitting curve.*

## 4. Discussion

As described in Sect 3.2.2., C K-edge NEXAFS spectroscopy provides a direct measure of the relative amount of $CaCO_3$ in various parts of the exoskeleton. Higher $CaCO_3$ content was found at the end of the claw (palm and finger), whereas a lower content was detected in the legs, especially their tips. Relatively high calcification ratio was revealed in the ventral part of the exoskeleton (pos. 1), while considerable variations were observed in the carapace. $CaCO_3$ in *C. granulata* does not adopt the aragonite structure detected in the *C. sapidus* (Katsikini, 2016) as it is confirmed

clearly from the absence of aragonite lattice modes in the Raman spectra as well as from the crystal field splitting of the Ca $L_2$- and $L_3$-edge peaks in the NEXAFS spectra. The formation of calcite crystallites on the carapace cuticle with an average size of 20 nm, was detected by TEM and the corresponding SAED patterns. The latter reveal a random or preferential orientation of the crystallites in the parts of the exocuticle and the bulges that originate from the endo- and penetrate the exo-cuticle, respectively. The absence of aragonite indicates that *C. Granulata* does not modify the mechanical properties of the exoskeleton by adopting the route of synthesis of a different crystalline polytype. Raman spectroscopy is proved very sensitive to the presence of an amorphous phase. Absence of the ACC phase was found in spots from the palm (RP1, RP2, RP4) and a tooth of the movable finger (RF2), whereas low crystallization ratios were detected in the three spots of the carapace (C1-C3). Furthermore, the Ca $L_{3,2}$-edge NEXAFS spectra are also proved sensitive to the crystalline or amorphous state of $CaCO_3$. In the latter case, the crystal field strength weakens causing a decrease of the separation between the main $L_2$ and $L_3$ peaks-along with a decreased intensity of the peaks appearing at their low-energy side. Direct comparison of the Ca $L_{3,2}$-edge NEXAFS spectra, recorded from different parts of the exoskeleton, with the spectrum of crystalline calcite shows clearly a close resemblance to the spectrum recorded from the movable finger (as far the intensity and the separation of the crystal field split peaks is concerned). The spectra recorded from other parts of the exoskeleton yielded more pronounced differences. A plot of the crystallization ratio obtained by Raman with the $L_2$ splitting yielded a linear dependence of the form:

(Crystallization ratio)=-3.01+3.28·($L_2$ splitting)

and can be used in order to determine the crystallization ratio from the characteristics of the NEXAFS spectra. Higher crystallization ratios were identified at the claw finger and lower values at the legs and the top of the carapace.

Both NEXAFS and Raman spectroscopies disclose significant variations in the calcification and crystallization of $CaCO_3$ in the exoskeleton of *C. granulata* studied here. Dillaman *et al.* (2007) studied the calcification process in the blue crab (*C. sapidus*) and found that calcium carbonate is first deposited as ACC and then transforms to a crystalline phase. On the other hand, in the American Lobster (*Homarus americanus*) cuticle, crystalline $CaCO_3$ has been detected only in the outer part of the exocuticle, whereas ACC prevails at the inner part of the exocuticle and the endocuticle (Al-Sawalmih *et al.*, 2009). Similar observations were made for the terrestrial crustaceans *Porcellio scaber*, *Armadillidium vulgare* and *Tyloseuropaeus Arcangeli* (Hild *et al.*, 2008; Seidl *et al.*, 2011). However, ACC was also found to play a structural role in isopods with the amount of crystalline $CaCO_3$ and ACC varying with depth in such a manner as to optimize the mechanical properties of the exoskeleton against predators (Hild *et al.*, 2009; Luquet, 2012). The detected variations in the calcification and crystallization ratios in the various parts of the exoskeleton of *C. granulata* can be related with the different function of each part. The end of the claw should be harder in order to grasp and crush food whereas legs should be more flexible and thus softer. The advantage of the presence of ACC, in combination with high concentration of organic material, in the cuticle is flexibility, plasticity and optimization of the strength and toughness whereas higher amounts of crystalline calcite impart hardness (Al-Sawalmih *et al.* 2009; Neues *et al.*, 2007). The hardness of the claw and the walking legs of the sheep crab (*Loxorhynchus grandis*)

has been measured by microindentation. The microhardness at the exocuticle region (located below the stained surface) was $947 \pm 74$ MPa and $247 \pm 19$ MPa for claws and walking legs, respectively, and it drops to about half of these values in the endocuticle (Chen et al, 2008), in line with our interpretation. Higher elastic modulus and nanohardness values were also determined in cuticle regions of *Tyloseuropaeus Arcangel* mineralised by calcite than in those mineralized by ACC (Seidl *et al.*, 2018). Therefore, our results strongly support the aspect that the ACC phase is not just a precursor of the crystalline phase, but it rather plays an important structural role where flexibility of the exoskeleton is necessary. The correlation coefficient between the calcification and the crystallization ratio is 0.52 suggesting a faint relation between the two different modifying mechanisms of the exoskeleton mechanical properties, i.e. higher $CaCO_3$ accumulation and its crystalline quality. However, an unambiguous conclusion towards this direction cannot be made yet.


## 5. Conclusions

Raman and NEXAFS spectra were recorded from different parts of the *Calappa granulata* exoskeleton in order to determine variations in the extent of crystallization and calcification. Raman spectra recorded from white regions exhibit only peaks attributable to $CaCO_3$ whereas in the spectra from colored parts the AXT chromophore characteristic peaks appear. In the main peak of $CaCO_3$ from the right palm and finger only a contribution from calcite is detected. However, in other parts of the exoskeleton a crystalline and an ACC phase coexist with their relative content varying at different parts of the exoskeleton. This probably dictates that the amorphous phase is not just a precursor of the crystalline phase, but it plays also a crucial role in the adjustment of the mechanical properties of the exoskeleton. The

Raman spectroscopy results are fully supported by the Ca $L_{3,2}$-edge NEXAFS spectroscopy. Variations observed in the intensity and the energy difference of the secondary peaks at the low-energy region of the $L_3$ and $L_2$ main peaks are consistent with the coexistence of an ACC phase and the crystalline one. The $L_2$ splitting correlates linearly to the crystallinity degree obtained by Raman spectroscopy, following the relation: (Crystallization ratio) = -3.01+3.28·($L_2$ splitting), enabling thus the estimation of the crystalline content in other calcified tissues, where calcite and ACC phases coexist. Variations are also observed in the calcification extent throughout the exoskeleton. The correlation between calcification and crystallization is found to be rather weak. The calcite structure of the crystalline $CaCO_3$ is also verified with TEM.

**References**

Albéric, M., Stifler, C. A., Zou, Z., Sun, C.-Y., Killian, C. E., Valencia, S., Mawass, M.-A., Bertinetti, L., Gilbert, P.U.P.A, Politi, Y., Growth and regrowth of adult sea urchin spines involve hydrated and anhydrous amorphous calcium carbonate precursors, J. Struct. Biol. X, 1, 100004 (2019).

Al-Sawalmih, A., Li, C., Siegel, S., Fratzl, P., Paris, O., 2009. On the Stability of Amorphous Minerals in Lobster Cuticle. Adv. Mater. 21, 4011–4015.

Addadi, L., Joester, D., Nudelman, F., Weiner, S., 2006. Mollusk shell formation: A source of new concepts for understanding biomineralization processes, Chem. Eur. J. 12, 980–987.

Aizenberg, J., Lambert, G., Addadi, L., Weiner, S., 1996. Stabilization of amorphous calcium carbonate by specialized macromolecules in biological and synthetic precipitates. Adv. Mater. 8, 222–226.

Baldwin, J., Johnsen, S., 2009. The importance of color in mate choice of the blue crab *Callinectes sapidus*. J. Exper. Biol. 212, 3762–3768.

Behrens, G., Kuhn, L.T., Ubic, R., Heuer, A.H., 1995. Raman spectra of vateritic calcium Carbonate. Spectrosc. Lett. 28, 983–995.

Beniash, E., Aizenberg, J., Addadi, L., Weiner, S., 1997. Amorphous calcium carbonate transforms into calcite during sea urchin larval spicule growth. Proc. R. Soc. Lond. Ser. B 264, 461-465.

Benzerara, K., Yoon, T.H., Tyliszczak, T., Constantz, B., Spormann, A.M., Brown, G. E., 2004. Scanning transmission X-ray microscopy study of microbial calcification. Geobiology 2, 249–259.

Bouligand, Y., 1972. Twisted fibrous arrangements in biological materials and cholesteric mesophases. Tissue and Cell 4,189–217.

Buchwald, M., Jencks, W.P., 1968. Properties of the crustacyanins and the yellow lobster shell pigment. Biochem. 7, 844–859.

Campbell, I. H., Fauchet P. M., 1986. The effects of microcrystal size and shape on the one phonon Raman spectra of crystalline semiconductors. Solid State Commun. 58, 739–741.

Cartwright, J.H.E., Checa, A.G., Gale, J.D., Gebauer, D., Sainz-Diaz, C.I., 2012. Calcium Carbonate Polyamorphism and Its Role in Biomineralization: How Many Amorphous Calcium Carbonates Are There? Angew. Chem. Int. Ed. 51, 11960–11970.

Chen, P.-Y., Lin, A.Y.-M., McKittrick, J., Meyers, M.A., 2008. Structure and mechanical properties of crab exoskeletons. Acta Biomater. 4, 587–596.

Cianci, M., Rizkallah, P.J., Olczak, A., Raftery, J., Chayen, N.E., Zagalsky, P.F., Helliwell, J.R., 2002. The molecular basis of the coloration mechanism in lobster shell: β-Crustacyanin at 3.2-Å resolution. Proc. Nat. Acad. Sci. 99, 9795–9800.

Cosmidis, J., Benzerara, K., Nassif, N., Tyliszczak, T., Bourdelle, F., Characterization of Ca-phosphate biological materials by scanning transmission X-ray microscopy (STXM) at the Ca $L_{2,3}$-, P $L_{2,3}$- and C K-edges. Acta Biomaterialia, 12, 260–269.

de Groot, F.M.F., Fuggle, J.C., Thole, B.T., Sawatzky, G.A., 1990. $L_{2,3}$ x-ray-absorption edges of $d^0$ compounds: $K^+$, $Ca^{2+}$, $Sc^{3+}$, and $Ti^{4+}$ in $O_h$ (octahedral) symmetry. Phys. Rev. B 41, 928–937.

de Groot, F., Kotani, A., 2008. Core Level Spectroscopy of Solids, CRC Press Taylor & Francis, Boca Raton.

Dillaman, R, Hequembourg, S., Gay, M., 2007. Early pattern of calcification in the dorsal carapace of the blue crab, *Callinectes sapidus*. J. Morphol. 263, 356– 374.

Fleet, M.E., Liu, X., 2009. Calcium L-2,L-3-edge XANES of carbonates, carbonate apatite, and oldhamite (CaS). Am. Mineral. 94, 1235–1241.

Gong, Y.U.T., Killian, C.E., Olson, I.C., Appathurai, N.P., Amasino, A.L., Martin, M.C., Holt, L.J., Wilt, F.H., Gilbert, P.U.P.A., 2012. Phase transitions in biogenic amorphous calcium carbonate, Proc. Natl. Acad. Sci. 109, 6088–6093.

Hadley, N. F., 1986. The Arthropod Cuticle. Sci. Am. 7, 98–106.

Hasse, B., Ehrenberg, H., Marxen, J.C., Becker, W., Epple, M., 2000. Calcium carbonate modifications in the mineralized shell of the freshwater snail *Biomphalaria glabrata*, Chem. Eur. J. 6, 3679–3685.

Hild, S., Marti, O., Ziegler, A., 2008. Spatial distribution of calcite and amorphous calcium carbonate in the cuticle of the terrestrial crustaceans *Porcellio scaber* and *Armadillidium vulgare*. J. Struct. Biol. 163, 100–108.

Hild, S., Neues, F., Žnidaršič, N., Štrus, J., Epple, M., Marti, O., Ziegler, A., 2009. Ultrastructure and mineral distribution in the tergal cuticle of the terrestrial isopod *Titanethes albus*. Adaptations to a karst cave biotope. J. Struct. Biol. 168, 426–436.

Jacob, D.E., Wirth, R., Soldati, A.L., Wehrmeister, U., Schreiber, A., 2011. Amorphous calcium carbonate in the shells of adult *Unionoida*. J. Struct. Biol. 173 241– 249.

Kaczor, A., Baranska, M., 2011. Structural changes of carotenoid astaxanthin in a single algal cell monitored *in situ* by Raman spectroscopy. Anal. Chem. 83, 7763– 7770.

Katsikini, M., 2016. Detailed spectroscopic study of the role of Br and Sr in coloured parts of the Callinectes sapidus crab claw. J. Struct. Biol. 195, 1–10.

Klepal, W., Rentenberger, C., Zheden, V., Adam, S., Gruber, D., 2010. Structural peculiarities of the penis of *Semibalanus balanoides* (Linnaeus, 1767) and *Chthamalus stellatus* (Poli, 1791) (Crustacea: Cirripedia: Thoracica). J. Exper. Mar. Biol. Ecol. 392, 228-233.

Konashuk, A.S., Samoilenko, D.O., Klyushin, A.Y., Svirskiy, G.I., Sakhonenkov, S.S., Brykalova, X.O., Kuzmina, M.A., Filatova, E.O., Vinogradov, A.S., Pavlychev, A. A., 2018. Thermal changes in young and mature bone nanostructure probed with Ca 2p excitations, Biomed. Phys. Eng. Express 4, 035031:1–8

Lam, R., Metzler, R., Gilbert, P., Beniash, E., 2012. Anisotropy of chemical bounds in collagen molecules studied by X-ray absorption near-edge structure (XANES) spectroscopy. ACS Chem. Biol. 7, 476–480.

Levi-Kalisman, Y., Raz, S., Weiner, S., Addadi, L., Sagi, I. , 2002. Structural differences between biogenic amorphous calcium carbonate phases using X-ray absorption spectroscopy. Adv. Funct. Mater. 12, 43–48.

Lowenstam, H. A., 1981. Minerals formed by organisms, Science 211, 1126–1131.

Luquet, G., 2012. Biomineralizations: insights and prospects from crustaceans. Zookeys. 176, 103–121.

Mergelsberg, S. T.; Ulrich, R. N.; Shuhai, X; Dove, P. M., 2019. Composition systematics in the exoskeleton of the american lobster, Homarus americanus and implications for malacostraca. Front. Earth Sci. 7, 69, 1-11.

Molodtsov, S.L., Fedoseenko, S.I., Vyalikh, D.V., Iossifov, I.E., Follath, R., Gorovikov, S.A., Brzhezinskaya, M.M., Dedkov, Y.S, Püttner, R., Schmidt, J.-S., Adamchuk, V.K., Gudat, W., Kaindl, G., 2009. High-resolution Russian-German beamline at BESSY. Appl. Phys. A 94, 501-505.

Nagasawa, H.,2012. The crustacean cuticle: Structure, composition and mineralization, Front. Biosci. (Elite Ed) 4, 711–720.

Nehrke, G., Poigner, H., Wilhelms-Dick, D., Brey, T., Abele, D., 2012. Coexistence of three calcium carbonate polymorphs in the shell of the Antarctic clam *Laternula elliptica*, Geochem. Geophys. Geosyst., 13, Q05014:1-8.

Neues, F., Ziegler, A., Epple, M., 2007. The composition of the mineralized cuticle in marine and terrestrial isopods: A comparative study. Cryst. Eng. Comm. 9, 1245–1251.

Neues, F., Hild, S., Epple, M., Marti, O., Ziegler, A., 2011. Amorphous and crystalline calcium carbonate distribution in the tergite cuticle of moulting *Porcellio scaber* (Isopoda, Crustacea). J. Struct. Biol. 175, 10-20.

Pavlychev, A.A., Avrunin, A.S., Vinogradov, A.S., Filatova, E.O., Doctorov, A.A., Krivosenko, Yu S., Samoilenko, D.O., Svirskiy, G.I., Konashuk, A.S., Rostov, D.A., 2016. Local electronic structure and nanolevel hierarchical organization of bone tissue: theory and NEXAFS study, Nanotechnology 27, 504002:1-8

Penel, G., Leroy, G., Rey, C., Bres, E., 1998. Micro-Raman Spectral Study of the $PO_4$ and $CO_3$ vibrational modes in synthetic and biological apatites. Calcif. Tissue Int. 63 475–481

Petrova, O.V., Nekipelov, S.V., Sivkov, D.V., Mingaleva, A E., Nikolaev, A., Frank-Kamenetskaya, O.V., Bazhenov, V.V., Vyalikh, D.V., Molodtsov, S.L., Sivkov, V.N., Ehrlich, H., 2017. Comparative NEXAFS study of the selected icefish hard tissues and hydroxyapatite, J. Phys.: Conf. Ser. 917, 042001:1–6.

Politi, Y., Metzler, R.A., Abrecht, M., Gilbert, B., Wilt, F.H., Sagi, I., Addadi, L., Weiner, S., Gilbert, P.U.P.A, 2008. Transformation mechanism of amorphous calcium carbonate into calcite in the sea urchin larval spicule. Proc. Natl. Acad. Sci. 45, 17362–17366.

Raz, S., Weiner, S., Addadi, L., 2000. Formation of high-magnesian calcites *via* an amorphous precursor phase: possible biological implications. Adv. Mater. 12, 38–42.

Rez, P., Blackwell A, 2011. Ca $L_{23}$ spectrum in amorphous and crystalline phases of calcium carbonate. J. Phys. Chem. 115, 11193–11198.

Rimai, L., Heyde, M.E., Gill, D., 1973. Vibrational spectra of some carotenoids and related linear polyenes. A Raman spectroscopic study. J. Am. Chem. Soc. 95, 4493–4501.

Rivera, S.M., Canela-Garayoa, R., 2012. Analytical tools for the analysis of carotenoids in diverse materials. J. Chromatogr. A 1224, 1–10.

Salares, V.R., Young, N.N., Bernstein, H.J., Carey, P.R., 1977. Resonance Raman spectra of lobster shell carotenoproteins and a model astaxanthin aggregate. A possible photobiological function for the yellow protein. Biochemistry 16, 4751–4756.

Salares, V.R., Young, N.M., Carey, P.R., Bernstein, H.J., 1977. Excited state (excitation) interactions in polyene aggregates. Resonance Raman and absorption spectroscopic evidence. J. Raman Spectrosc. 6, 282–288.

Seidl, B., Huemer, K., Neues, F., Hild, S., Epple, M., Ziegler, A., 2011. Ultrastructure and mineral distribution in the tergite cuticle of the beach isopod *Tylos europaeus Arcangeli*, 1938. J. Struct. Biol. 174, 512–526.

Seidl, B.H.M., Ziegler, A., 2012. Electron microscopic and preparative methods for the analysis of isopod cuticle. ZooKeys 176 73–85.

Seidl, B.H.M., Griesshaber, E., Fabritius, H.-O., Reisecker, C., Hild, S., Taiti, S., Schmahl, W.W., Ziegler, A., 2018. Tailored disorder in calcite organization in tergite cuticle of the supralittoral isopod *Tylos europaeus Arcangeli*, 1938, J. Struct. Biol., 204, 464-480.

Stöhr, J., 2003. NEXAFS Spectroscopy, Springer, Berlin.

Stavitski, E., de Groot, F.M.F., 2010. The CTM4XAS program for EELS and XAS spectral shape analysis of transition metal L edges. Micron 41, 687–694.

Štrus, J., Tušek-Žnidarič, M., Repnik, U., Blejec, A., Summers, A., 2019. Microscopy of crustacean cuticle: formation of a flexible extracellular matrix in moulting sea slaters *Ligia pallasii*, J. Mar. Biol. Assoc. UK, 99, 857-865.

Tilley, R.J.D., 2011. Colour and the optical properties of materials, second ed., J. Wiley& Sons, Chichester.

Tsao, C., Yu, P.-T., Lo, C.-H., Chang, C.-K., Wang, C.-H., Yang, Y.-W., Chan, J.C.C., 2019. Anhydrous amorphous calcium carbonate (ACC) is structurally different from the transient phase of biogenic ACC. Chem. Commun. 55,6946–6949

Vittori, M., Kostanjšek, R., Žnidaršič, N., Žagar, K., Čeh, M., Štrus, J., 2012. Calcium bodies of *Titanethes albus* (Crustacea: Isopoda): Molt-related structural dynamics and calcified matrix-associated bacteria, J. Struct. Biol. 180, 216-225.

Waddy, S. L., Aiken, D.E., De Kleijn, D.P.V., 1995. Control of Growth and Reproduction in Biology of the Lobster, Ch.10, Academic Press, San Diego.

Weesie, R.J., Merlin, J.C., Lugtenburg, J., Britton, G., Jansen, F.J.H.M., Cornard, J.P., 1999. Semiempirical and Raman spectroscopic studied of carotenoids. Biospectroscopy 5, 19–33.

Wehrmeister, U., Jacob, D.E., Soldati, A.L., Loges, N., Häger, T., Hofmeister, W., 2011. Amorphous, nanocrystalline and crystalline calcium carbonates in biological materials, J. Raman Spectrosc. 42, 926 – 935.

Weiner, S., Levi-Kalisman, Y., Raz, S., Addadi, L., 2003. Biologically Formed Amorphous Calcium Carbonate, Connect. Tissue Res. 44, 214–218.

Weiss, I. M., Tuross, N., Addadi, L., Weiner, S., 2002. Mollusc larval shell formation: amorphous calcium carbonate is a precursor phase for Aragonite. J. Exp. Zool. 293 478–491.

Zougrou, I.M., Katsikini, M., Brzhezinskaya, M., Pinakidou, F., Papadopoulou, L., Tsoukala, E., Paloura, E.C., 2016. Ca $L_{2,3}$-edge XANES and Sr K-edge EXAFS study of hydroxyapatite and fossil bone apatite, Sci. Nat. 103, 60:1–12.